



Epitaxial diamond on Ir/ SrTiO₃/Si (001): From sequential material characterizations to fabrication of lateral Schottky diodes

Jean-Charles Arnault, K.H. Lee, Julien Delchevalrie, J. Penuelas, L. Mehmel, O. Brinza, S. Temgoua, I. Stenger, J. Letellier, G. Saint-Girons, et al.

► To cite this version:

Jean-Charles Arnault, K.H. Lee, Julien Delchevalrie, J. Penuelas, L. Mehmel, et al.. Epitaxial diamond on Ir/ SrTiO₃/Si (001): From sequential material characterizations to fabrication of lateral Schottky diodes. *Diamond and Related Materials*, 2020, 105, pp.107768. 10.1016/j.diamond.2020.107768 . hal-02500531

HAL Id: hal-02500531

<https://hal.science/hal-02500531>

Submitted on 19 Mar 2020

HAL is a multi-disciplinary open access archive for the deposit and dissemination of scientific research documents, whether they are published or not. The documents may come from teaching and research institutions in France or abroad, or from public or private research centers.

L'archive ouverte pluridisciplinaire **HAL**, est destinée au dépôt et à la diffusion de documents scientifiques de niveau recherche, publiés ou non, émanant des établissements d'enseignement et de recherche français ou étrangers, des laboratoires publics ou privés.

Diamond on Ir / SrTiO₃ / Si (001): from sequential material characterizations to fabrication of lateral Schottky diodes

J. C. Arnault^{1*}, K. H. Lee¹, J. Delchevalrie¹, J. Penuelas², L. Mehmel³, O. Brinza³, S. Temgoua⁴, I. Stenger⁴, J. Letellier⁵, G. Saint-Girons², R. Bachelet², R. Issaoui³, A. Tallaire³, J. Achard³, J. Barjon⁴, D. Eon⁵, C. Ricolleau⁶, S. Saada¹

¹CEA, LIST, Diamond Sensors Laboratory, 91191, Gif-sur-Yvette, France

² INL, CNRS UMR 5270, Université de Lyon, Ecole Centrale de Lyon, F-69134 Ecully, France

³LSPM, Université Paris 13, Sorbonne Paris Cité, CNRS, Villetaneuse 93430, France

⁴GEMAC, Université Versailles St Quentin en Yvelines, CNRS, Université Paris Saclay, 78000 Versailles, France

⁵Univ. Grenoble Alpes, CNRS, Grenoble INP*, Institut Néel, 38000 Grenoble, France

⁶MPQ, Université de Paris, CNRS, UMR 7162, Bâtiment Condorcet, 75013 Paris, France

* Corresponding author: jean-charles.arnault@cea.fr

Abstract

Advanced characterizations with combined analytical tools were carried out at the different stages of diamond heteroepitaxy on Ir/STO/Si (001) substrates. HRTEM and STEM-EELS revealed the presence of epitaxial nanometric diamond crystals after BEN. UV Raman allowed estimating the diamond film quality and its strain at the early stages of heteroepitaxial growth. The crystalline structure and the strain within thick heteroepitaxial films were determined by XRD and CL investigations. A CL study of the cross-section provided the mapping of the dislocation network along the growth direction. Measurements performed on lateral Schottky diodes fabricated on a thick diamond film showed an excellent reproducibility on the substrate with a Schottky barrier height in good agreement with those obtained on homoepitaxial layers.

Highlights:

- Characterizations at different stages of heteroepitaxy combining complementary analytical tools were performed to relate the electrical properties to the structural ones.
- After BEN and without CVD growth, diamond nuclei are evidenced by HRTEM and STEM-EELS
- UV Raman allows to estimate the diamond film quality at the early stages of heteroepitaxial growth
- Measurements on lateral Schottky diodes showed an excellent reproducibility on the substrate
- Schottky barrier height in good agreement with those obtained on homoepitaxial layers
- Heteroepitaxially grown diamond films show similar boron incorporation efficiency as standard homoepitaxial ones.

Keywords

Iridium, Diamond Heteroepitaxy, Interfaces, Schottky diodes

1. Introduction

Diamond heteroepitaxy on iridium becomes a credible alternative to single crystal diamond materials obtained by homoepitaxial growth by Chemical Vapor Deposition (CVD) or by High Pressure High Temperature (HPHT). Indeed, the last report of Ichikawa et al. that used a patterning approach allowing Epitaxial Lateral Overgrowth (ELO) demonstrated a crystalline quality comparable to homoepitaxial diamond with dislocations density within the $10^6\text{-}10^7\text{ cm}^{-2}$ range [1]. Moreover, the few research groups involved in diamond heteroepitaxy used scalable substrates like MgO, α -Al₂O₃ or silicon-based substrates for iridium deposition. In 2017, Schreck et al. showed a 90 mm diamond heteroepitaxial wafer grown on Ir/YSZ/Si(001) [2]. Such heteroepitaxial diamond may have future applications for detection, photonics and electronic devices.

In our previous report, we demonstrated that Ir/SrTiO₃(STO)/Si(001) up-scalable substrates are also very promising for diamond heteroepitaxy [3]. Indeed, the reported crystalline quality of 1.5 μm thick films investigated by X-Ray Diffraction (XRD) is at the state of the art for comparable thickness. To further improve the crystallinity of thick heteroepitaxial films, the present study provides a sequential approach with structural and chemical investigations performed after the successive steps of the heteroepitaxy process: the Bias Enhanced Nucleation (BEN), the growth of thin diamond epilayers, the thickening of these films under homoepitaxial CVD conditions. Complementary techniques like Scanning Electron Microscopy (SEM), High Resolution Transmission Electron Microscopy (HRTEM), Scanning TEM Electron Energy Loss Spectroscopy (STEM-EELS), XRD, Cathodoluminescence (CL) and Raman spectroscopy were combined to measure the crystalline quality, the strain and the defects distribution within heteroepitaxial diamond films grown on Ir/STO/Si(001).

The impact of defects on the performance of devices is material dependent. The case of GaN is emblematic: laser, LED and transistors are commercially available despite a high dislocation density [4, 5] ($10^8\text{-}10^{10}\text{ cm}^{-2}$) compared to other semiconductor devices. The present work also aims to evaluate if the state-of-the-art quality of heteroepitaxial diamond on iridium is sufficient for making a simple electronic device, such as a p-type lateral Schottky diode. Such electronic devices were fabricated and characterized on a thick heteroepitaxial film grown on Ir/STO/Si(001).

2. Experimental

Two kinds of SrTiO₃ (001) (STO) substrates were used in the present study for the subsequent epitaxial growth of iridium and diamond layers. The first one is a STO thin film grown by Molecular Beam Epitaxy (MBE) onto 500 μm -thick (001)-oriented silicon wafers. The second one, a 500 μm -thick STO single crystal supplied from CrysTec Inc, is mainly used as a reference and for the TEM study of the diamond nucleation.

2.1 STO pseudo-substrate on Si(001)

The MBE deposition was achieved using Knudsen effusion cells for Sr and Ti evaporation in co-deposition. The growth temperature, oxygen partial pressure $P(\text{O}_2)$ and growth rate were 400°C, 6.6×10^{-8} mbar and 1.5 ML/min, respectively. After preparation of the Sr-passivated Si (001) surface [6], the STO growth was started using a slight Sr excess for optimal crystallization and epitaxy at this moderate temperature [7]. Stoichiometry conditions were re-established after a few monolayers. About 40 nm thick STO/Si films were used here for further deposition of epitaxial Ir and diamond layers. Additional details about the STO/Si growth process by MBE can be found elsewhere [3, 7-8]. The crystalline quality, the thickness and the morphology of the STO/Si films were assessed using *in situ* Reflection High-Energy Electron Diffraction (RHEED), XRD, X-Ray Reflectometry (XRR), Atomic Force Microscopy (AFM) and Field Emission SEM (FE-SEM).

Figure 1 shows the structural characterization of the epitaxial STO layer on Si(001). The bright periodic streaks in RHEED patterns attest to the good epitaxial quality of the layer (Fig. 1a). Some spots along the streaks reveal that the surface is slightly rough. However, the mean surface and STO/Si interface RMS roughnesses measured by XRR are quite low (about 0.6 nm and 0.75 nm, respectively), and fringes are sustainably observed on the XRR spectrum beyond 3° (Fig. 1b). The difference between the fit and the experimental data are most probably due to a composition gradient across the film thickness because of Sr enrichment in the early stages of STO growth on Si [7] and Sr surface segregation in STO [9, 10]. However, the measured thickness of exactly 38.6 nm here is reliable with a good correspondence of the intensity maxima between the fit and the experimental data.

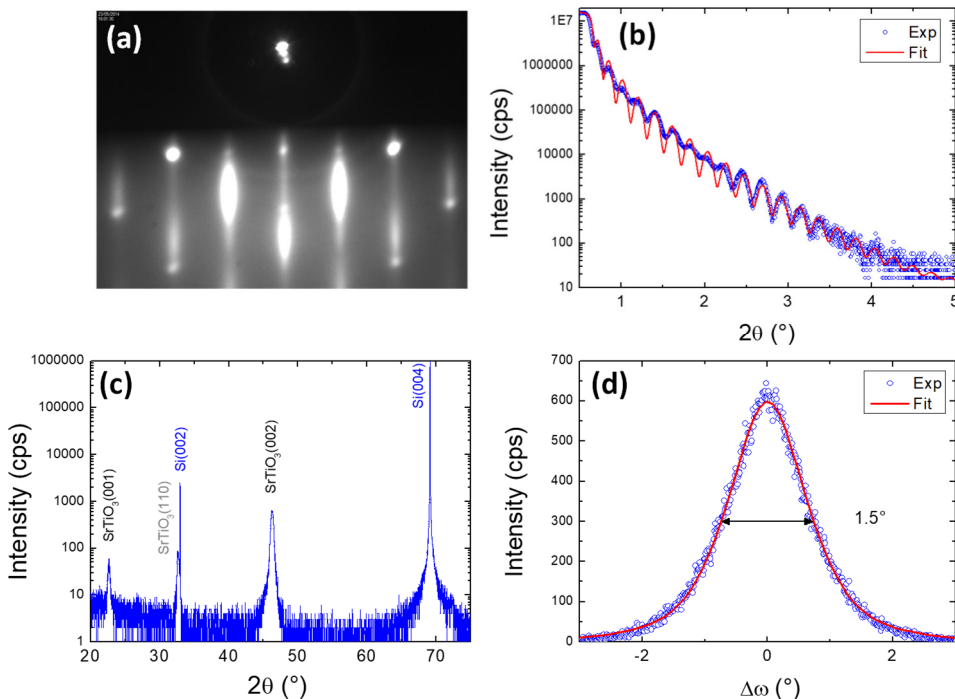


Figure 1: Structural characterization of the STO/Si substrate. (a) RHEED pattern recorded along the $<100>_{\text{STO}}$ direction at the end of the growth, (b) XRR, (c) XRD $\theta/2\theta$ scan, and (d) XRD ω -scan around the (002) reflection of STO.

As expected and shown by the XRD $\theta/2\theta$ scan, the STO/Si epitaxial layer is (001)-oriented (Fig. 1c). A small fraction of (110)-oriented domains is also detected (about 4.2% for this film). The mosaicity of the layer is around 1.5° (Fig. 1d), which is a reasonable value considering the challenging epitaxy of similar oxide layers on Si.

2.2 Epitaxy of iridium on STO substrates

Iridium epilayers were deposited by e-beam evaporation onto both STO substrates. For bulk STO, the following deposition conditions were used: at 900°C with an iridium deposition rate of 2 nm/min under a pressure of $9.0 \times 10^{-7}\text{ mbar}$ [11]. An 80 nm thick iridium epilayer was deposited onto the STO/Si (001) substrate of $5 \times 5\text{ mm}^2$. The suitable deposition conditions were adjusted taking into account the thermal stability of the STO layer [3]. The deposition rate was 1 nm/min under a pressure lower than 10^{-6} mbar at 660°C , measured by an infrared pyrometer ($1.45\text{--}1.8\text{ }\mu\text{m}$) with 0.57 for emissivity. The surface morphology was checked by FE-SEM and the presence of square-shape nanocrystals aligned along the [011] directions is in line with the epitaxy of the iridium film (Fig. S1). The XRD $\theta/2\theta$ scan of the Ir/STO/Si(001) heterostructure is shown in Figure 2a. As targeted, the Ir layer is predominantly (001)-oriented on STO/Si(001). Only a very limited trace of $(111)_{\text{Ir}}$ orientation is detected (estimated to be less than 1%). Figure 2b shows a zoom of this scan around the $(111)_{\text{Ir}}$ and $(002)_{\text{Ir}}$ reflections. The peak positions are very close to the bulk Bragg positions with a slight difference of $+0.1^\circ$ on (002) diffraction peak in 2θ , corresponding to a reduction of the out-of-plane lattice parameter of 0.008 \AA (0.2% strain), that can be well explained by the thermal expansion coefficient difference between the Ir film and silicon substrate (yielding slight in-plane tensile stress to the film) [12]. Indeed, the Thermal Expansion Coefficients (TEC) are $6.4 \cdot 10^{-6}\text{ K}^{-1}$ and $2.6 \cdot 10^{-6}\text{ K}^{-1}$ for iridium and silicon, respectively. This TEC difference gives an in-plane tension of around +0.3% ($a \sim 3.85\text{ \AA}$), with this 660°C growth temperature, and yielding a lattice reduction of -0.2%, considering both the Ir Poisson ratio of 0.26 and biaxial stress [13]. By fitting the peaks and taking into account the structural factor difference between reflections, evaluation of the orientation ratio reveals that the $(111)_{\text{Ir}}$ orientation represents only < 0.04% of the Ir layer.

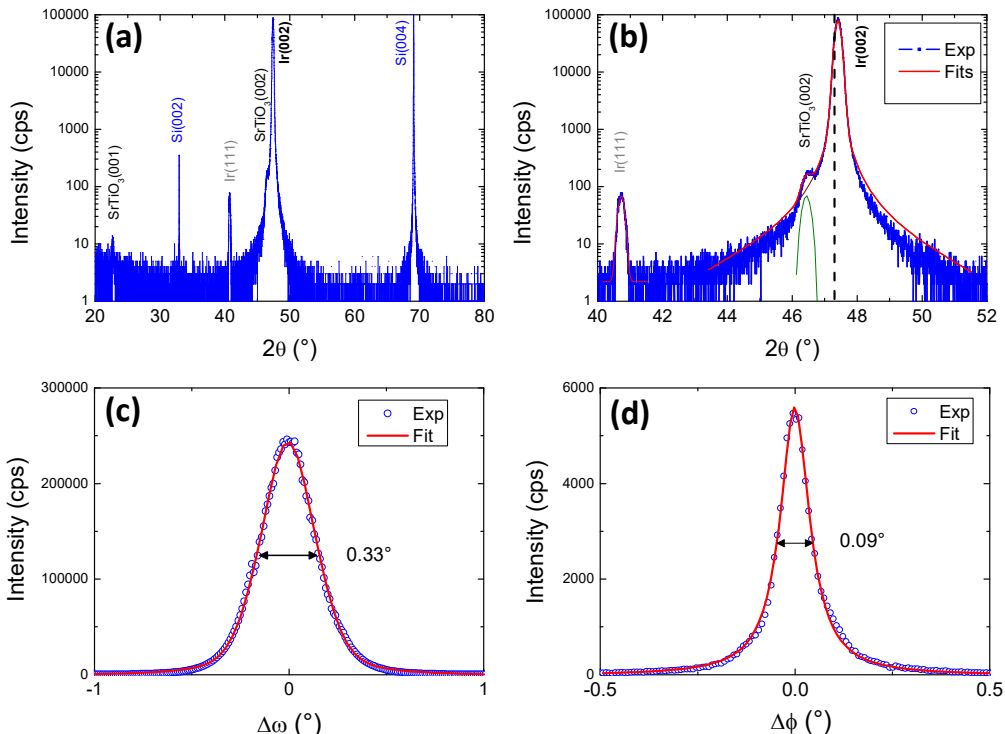


Figure 2: XRD characterization of Ir/STO/Si(001) heterostructure: (a) large $\theta/2\theta$ scan, (b) $\theta/2\theta$ scan focused on the $(111)_{\text{Ir}}$ and $(002)_{\text{Ir}}$ reflections (vertical black dashed line indicates the position of the bulk $\text{Ir}(002)$ reflection), (c) ω -scan around the $(002)_{\text{Ir}}$ reflection, (d) ϕ -scan around the $(200)_{\text{Ir}}$ reflection at the surface region in grazing incidence configuration (GIXRD).

The polar mosaicity measured around the $(002)_{\text{Ir}}$ reflection by ω -scan (0.33° as shown in Fig. 2c) is relatively low. The azimuthal (in-plane) mosaicity measured around the $(200)_{\text{Ir}}$ reflection by ϕ -scan at the surface region of the layer in grazing incidence configuration (GIXRD), as shown in Figure 2d, is even lower, namely less than 0.1° .

2.3 Bias Enhanced Nucleation of diamond

The BEN step was performed in a Microwave Plasma CVD (MPCVD) reactor. This nucleation method was previously applied to Ir/STO (001) samples and further adapted to Ir/STO/Si (001) substrates [14]. Both Ir/STO (001) and Ir/STO/Si (001) samples underwent the following BEN parameters during 45 min: bias voltage - 307 V; microwave power 400 W; gas pressure 20 mbar; temperature 700°C ; CH_4 content 4 vol.% in H_2 . More details about the BEN technique were previously provided [3, 11, 15]. The Ir/STO (001) after BEN was used to prepare a cross-section lamella to investigate the interface by HRTEM (see part 2.5) while a diamond film was grown onto the Ir/STO/Si (001) sample.

2.4 Heteroepitaxial diamond growth

After BEN, three CVD syntheses were applied to grow the heteroepitaxial diamond film on the Ir/STO/Si(001) sample. A first CVD growth of 2 h was performed in the same MPCVD reactor with the following experimental conditions: microwave power 400W; gas pressure 20 mbar; CH_4 content 0.6 vol. % in H_2 . A second step consisting in thickening the diamond layer, in another MPCVD reactor, up to several hundreds of microns was performed by using optimized growth conditions [16] developed for homoepitaxial growth: microwave power 3000W; temperature 900°C ; gas pressure 200 mbar; CH_4 content 4 vol. % in H_2 .

Eventually, to assess the electronic properties of lateral Schottky diodes, a low boron doped overlayer was grown onto the polished thick heteroepitaxial film following a recipe previously developed for homoepitaxial growth and a doping at 10^{16} cm^{-3} . After cleaning in a boiling tri-acid mixture (HClO_4 , HNO_3 and H_2SO_4 in a proportion 1:4:3), the previous intrinsic heteroepitaxial diamond layer underwent a hydrogen plasma during 2 h. The recipe used to grow the boron doped epilayer corresponds to a boron over carbon ratio of 60 and with 0.25% of oxygen in the mixture. The growth conditions applied during 2 h were: gas pressure 44 mbar; temperature 900°C .

2.5 Characterization techniques

The scanning electron microscopy was mainly carried out using a FE-SEM ZEISS SUPRA 40 equipped with an in-lens detector.

The crystalline quality (orientation, mosaicity, strain) of the different layers was investigated by XRD. A high-resolution Rigaku SmartLab X-ray diffractometer, equipped with a 9 kW copper rotating anode and a two-bounce Ge(220) monochromator with $\lambda_{\text{CuK}\alpha 1} = 1.54056 \text{ \AA}$, was used.

For CL in the UV range, a JEOL 7001F FE-SEM was used. Samples were cooled down to 10 K and the CL spectrum and images were recorded with an optical detection system already detailed in Ref. [17]. The 10 kV electron beam energy used in this work corresponds to a $\sim 0.9 \mu\text{m}$ stopping depth for electrons in diamond [18].

A table-top CL system which uses a much larger electron beam ($\sim 7 \text{ mm}$, $\sim 10 \text{ keV}$) is also used to excite the diamond samples at room temperature and to collect their CL in the visible range with a CCD camera mounted on a microscope records color CL images, as used in mineralogy sciences. Photoluminescence images are also taken with the commercial DiamondView system. Both analysis are complementary since DiamondViewTM images give insights on volume defects, while the electron beam excitation probes only the sub-surface region.

For HRTEM analysis, lamellae were prepared from two samples using a dual beam Focus Ion Beam (FIB) FEI Helios 600 Nanolab: (i) for a better identification of diamond nucleation, a TEM lamella was first fabricated from the Ir/STO(001) sample just after the BEN step; (ii) a second cross-section was prepared from the diamond film grown during 2 h. During the preparation of these lamellae, nanocrystalline platinum film, which can be observed on the HRTEM images, was locally deposited by electron beam assisted CVD, in order to protect the material of interest. HRTEM was performed on a cold FEG Jeol ARM200F microscope equipped with a CEOS aberration corrector of the objective lens. At 200 keV, the point to point resolution is 75 pm. The EELS spectrum was acquired with an HRTEM Jeol 2010 equipped with a GIF 2000 and a STEM mode. Both microscopes were operated at 200 keV.

Raman measurements were performed in backscattering geometry with an UV laser excitation at 325 nm and using a high-resolution Raman spectrometer setup HORIBA Jobin-Yvon Labram HR800. With the $40 \times$ UV objective and $2400 \text{ lines.mm}^{-1}$ grating used, each pixel of the charge-coupled detector (CCD) covers 1 cm^{-1} .

2.6 Electrical characterization of lateral Schottky diodes

The lateral Schottky diodes were characterized inside a probe station able to work under vacuum (pressure below 10^{-3} mbar) with a controlled temperature. Current-voltage (I-V) measurements were performed with a Keithley 6517B under vacuum at room temperature. Capacitance-voltage (C-V) measurements were measured with a Modulab XM MTS system in the same conditions.

3. Results

3.1 Bias Enhanced Nucleation

FE-SEM images of the iridium surface after BEN reveals the presence of domains appearing as brighter areas (Fig. 3) in which diamond *nuclei* were previously evidenced tuning the observation conditions [11]. The nucleation domains are observed in both samples, either on epitaxial Ir/STO or on epitaxial Ir/STO/Si(100). Their shape and density extracted from FE-SEM pictures though look very different: for the Ir/STO/Si(001) after BEN, the domain density is higher than $1 \times 10^9 \text{ cm}^{-2}$ and the domain shape looks fractal (Fig. 3a). This corresponds to a surface coverage ratio of 21 %. For the Ir/STO (001), the domains are rounded with a density of $1 \times 10^8 \text{ cm}^{-2}$ (Fig. 3b).

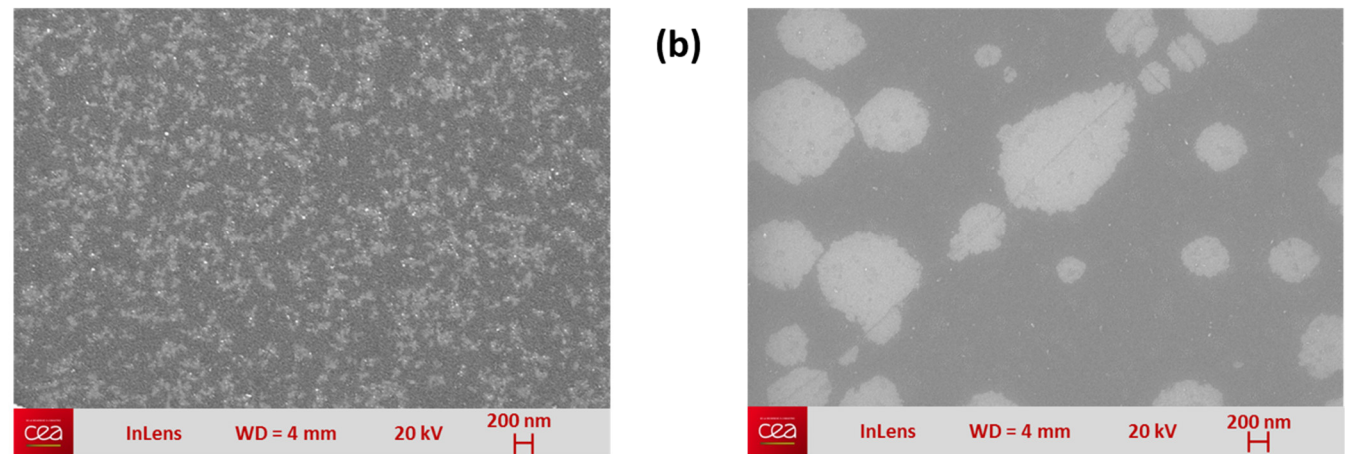


Figure 3: FE-SEM observations of domains after BEN on (a) Ir/STO/Si (001); (b) Ir/STO (001)

The Ir/STO (001) sample exposed to the BEN process was further investigated by cross-sectional HRTEM. In Fig. 4, a diamond nanocrystal with a lateral size of 7 nm and a height of 2.7 nm formed at the surface of the Ir monocrystalline epilayer is clearly observed, directly after the BEN step (highlighted by a white contour). The carbon K-edge EELS spectrum recorded on such a nanocrystal confirms it is made of diamond, with the typical signature of a σ^* feature located from 290 eV to 310 eV corresponding to carbon in sp^3 coordination (Fig. 4c) [19].

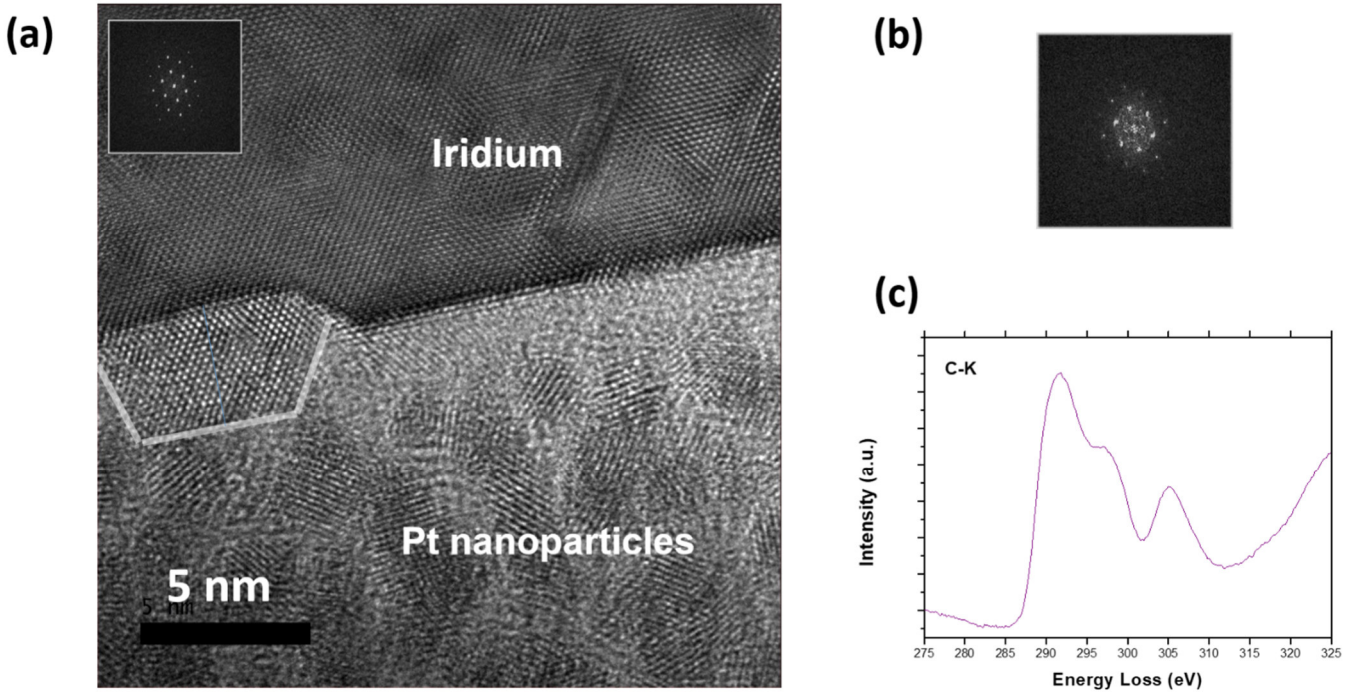


Figure 4 (a) HRTEM bright field image of a diamond nanocrystal at the surface of the Ir monocrystalline epilayer which underwent the BEN step. This nanocrystal is identified by a white contour; Platinum nanoparticles from the protective coating are observed on the HRTEM image. (b) Fast Fourier Transform of the HRTEM image of the diamond nanocrystal; (c) C-K EELS spectrum recorded on such a nanocrystal.

The comparison of the Fast Fourier Transforms (FFT) of the diamond crystal (Fig. 4b) and of the iridium film (insert Fig. 4a) shows that the diamond nanocrystal is perfectly oriented on the iridium surface. The corresponding zone axis is $<110>$. The epitaxial relationship is diamond (002) [220] // iridium (002) [220]. The angle between the top face and the lateral face of the nanocrystal is close to 54° which corresponds to the angle between (100) and (111) crystallographic directions showing that the diamond crystal is (002) oriented with lateral (111) faces. This diamond nanocrystal nucleated close to a furrow formed on Ir monocrystalline film during the BEN step [11]. The diffractogram of the iridium film was used to precisely calibrate the magnification of the electron microscope. We found for the diamond nanocrystal: $d_{220} = 0.136$ nm and $d_{002} = 0.192$ nm which gives a unit cell parameter $a = 0.381$ nm, i.e. very close to the unit cell parameter of iridium ($a = 0.383$ nm). This result indicates that the diamond nanocrystal is in a biaxial tension in comparison with bulk diamond ($a = 0.357$ nm) with an in-plane tensile strain of about +7%.

3.2 Growth of thin diamond epilayers

The Ir/STO/Si (001) sample, containing diamond nuclei after the BEN step, underwent a diamond growth of 2 h (see conditions in the experimental section), resulting in a film thickness of 310 nm (Fig. 6). The SEM image of the surface shows a nearly coalesced film exhibiting smooth top facets corresponding to a (001) orientation with

borders oriented towards $\{110\}$ directions (Fig. S2). To investigate the crystalline quality of the epitaxial film, Raman spectroscopy was performed. Note that the first order diamond Raman peak is generally undetectable with the classical visible wavelengths (like 514 nm) for such thin layers of heteroepitaxial diamond. Nevertheless, the UV excitation at 325 nm led to the exaltation of the Raman scattering. Under these conditions, the first order Raman diamond peak could be detected, located at 1330 cm^{-1} with a full width at half maximum (FWHM) of 18 cm^{-1} (Fig. 5). Its shifted frequency position and large linewidth indicates a slightly strained diamond with dominant tensile stress [20]. The presence of the G band at 1600 cm^{-1} is probably related to the non-diamond carbon located within the grain boundaries visible on the FE-SEM image of Fig. S2.

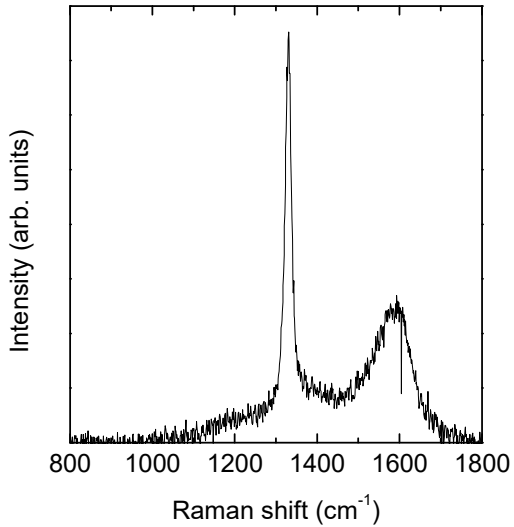


Figure 5 Raman spectrum of the 310 nm-thick diamond heteroepitaxial layer grown on Ir/STO/Si (100). UV laser excitation at 325 nm.

The TEM analysis of the diamond/Ir/STO/Si (001) multilayer is presented in Fig. 6. The TEM image provides an overview of the full stacking of epitaxial layers from the silicon substrate to the 310 nm thick diamond film. Diamond crystals have grown along the (001) axis with (111)-oriented lateral facets which are partially coalesced. Grain boundaries can still be observed between the diamond crystals at this stage. HRTEM images are depicted on Fig. 7 along the $\langle 110 \rangle$ zone axis. At the interface between diamond and iridium, no sp^2 carbon layer could be detected, which means that diamond is epitaxially grown on Ir in a direct way, i.e. without an intermediate layer. Moreover, for such a thin layer, dislocations and twins are clearly observed due to the lattice mismatch existing between diamond and iridium lattices, responsible for the strain already evidenced by Raman (Fig. 5). The analysis of the diamond interplanar spacing (d_{hkl}), measured with the FFT of HRTEM images, is performed in two regions: close to the diamond/iridium interface and within the diamond film. The results are presented in Table 1. The two sets of interplanar distances are very similar to each other and very close to the distances in a fully relaxed bulk diamond, at least within the uncertainty of atomic distance measurements from HRTEM images ($\pm 0.005\text{ nm}$). The diamond thin film appears to be completely relaxed.

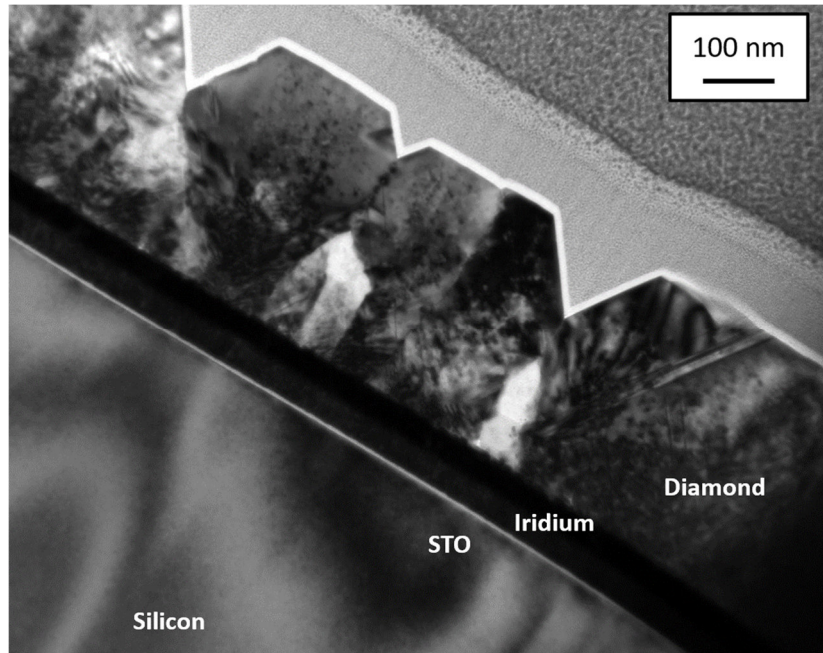


Figure 6 TEM bright field image of the full stacking of the diamond/Ir/STO/Si (001) sample

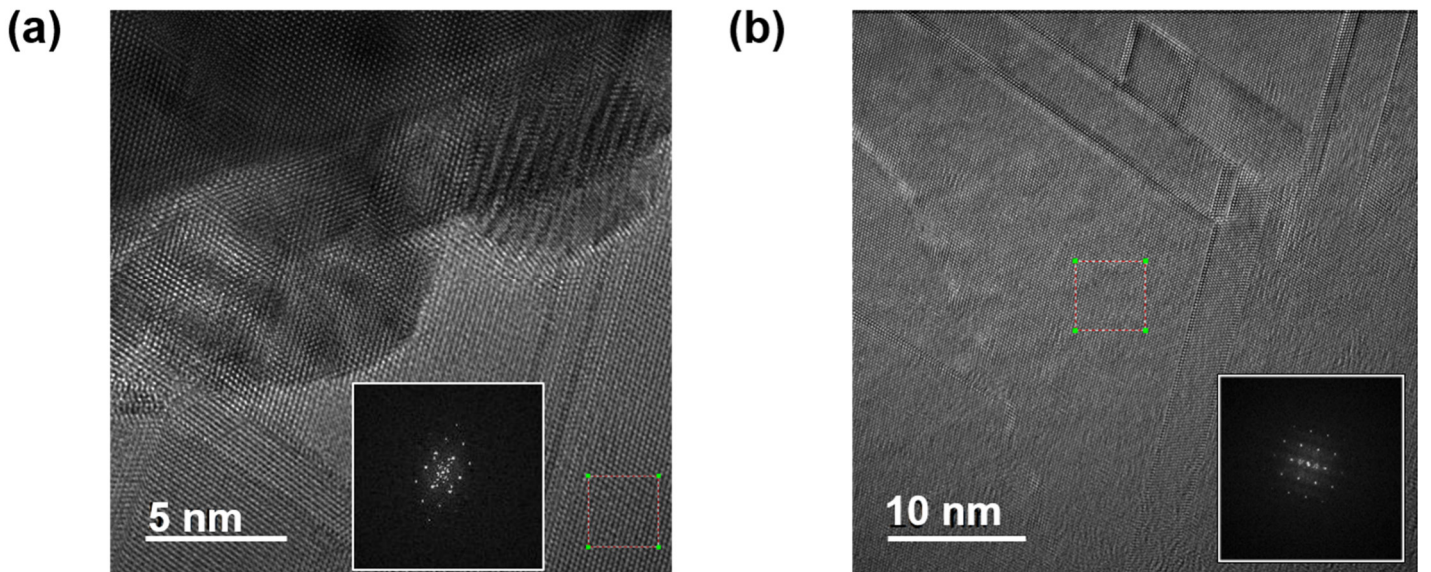


Figure 7 HRTEM bright field images taken along the $<110>$ zone axis (a) at the diamond/Ir interface; (b) inside the diamond film at 100 nm from the diamond/Ir interface. Insets showed FFT extracted from the squared area indicated with red dotted lines.

Table 1: Interplanar spacings in the diamond nanocrystal (Fig. 4a), in the diamond epilayer as measured from FFT performed at the interface (Fig. 7a) and 100 nm far from the interface (Fig. 7b). The reference values of the relaxed diamond lattice are given for comparison.

	diamond nanocrystal	interface diamond/Ir	100 nm from the interface	relaxed diamond
d_{002}	0.192 nm	0.178 nm	0.182 nm	0.178 nm
d_{111}	0.222 nm	0.209 nm	0.207 nm	0.206 nm
d_{220}	0.136 nm	0.128 nm	0.126 nm	0.126 nm

3.3 Thick diamond crystal obtained with homoepitaxial growth conditions

A thick diamond film of 240 μm was grown using CVD conditions optimized for the homoepitaxy of diamond on IIa substrates (see Part 2.4). The wide XRD $\theta/2\theta$ scan of the diamond/Ir/STO/Si (001) heterostructure is shown on Figure 8a.

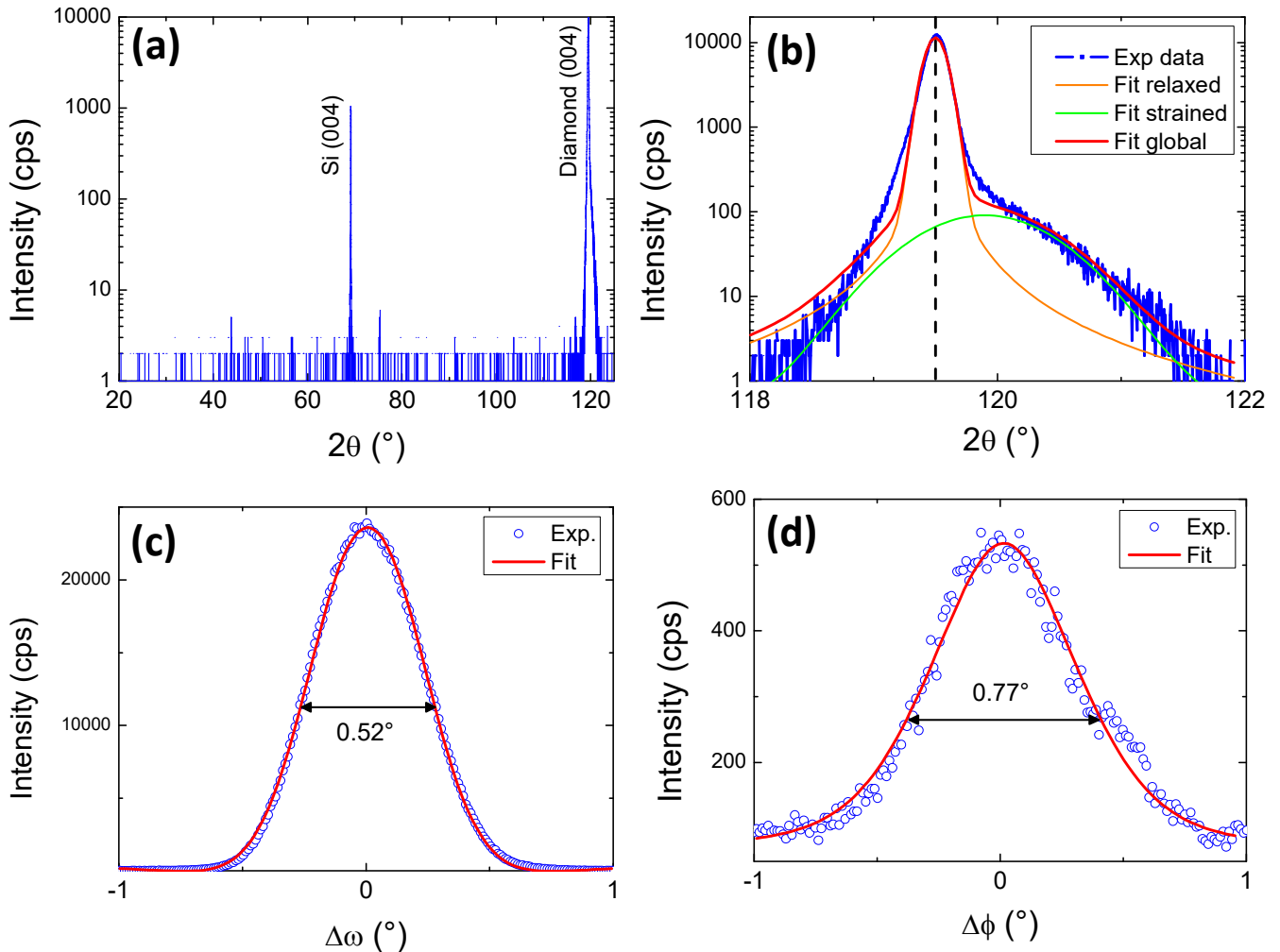


Figure 8 XRD characterization of epitaxial diamond layer grown on Ir/STO/Si(001): (a) large $\theta/2\theta$ scan; (b) $\theta/2\theta$ scan focused on the (004) reflection of diamond; (c) ω -scan around the (004) reflection of the diamond; (d) ϕ -scan around the (220) reflection of the diamond at the surface region in GIXRD.

As targeted, the diamond layer appears fully (001)-oriented on Ir/STO/Si (001), which is the expected signature for a monocrystalline film. Figure 8b shows a zoom of this scan around the (004) reflection of the diamond. The main peak is centered at the bulk Bragg position (indicated by the vertical dashed line) showing that the diamond layer is mainly relaxed ($c = 3.567 \text{ \AA}$). However, this peak presents a broad shoulder of low intensity at higher 2θ angles. This shows that a minority portion of the diamond layer has a cell parameter in the out-of-plane direction slightly lower than the bulk value. This can be probably caused by residual strain from the growth process and epitaxy at high temperature (in-plane tensile strain of about +7% from lattice mismatch). A deconvolution of the peak shows that this residual strained portion of the film represents less than 5% of the film, has a mean out-of-plane cell parameter $c = 3.559 \text{ \AA}$ (corresponding to a mean reduction of -0.2% respect to the bulk value). However, the large width of this shoulder indicates a relatively wide distribution of the cell parameter of this strained portion of around $\pm 0.009 \text{ \AA}$, corresponding to a strain distribution from 0 % to -0.5%. This strain

distribution may appear during the growth along the film thickness, in coherence with CL observations (see below). A similar result was previously observed on heteroepitaxial diamond layers on Ir/STO (001) substrates [17], although the thermal expansion coefficient mismatch here on Si substrate is lower than on STO substrate [12]. The polar mosaicity measured around the (004) reflection by ω -scan, as shown in Figure 8c, is low (0.52°). The azimuthal (in-plane) mosaicity measured around the (220) reflection by ϕ -scan at the surface region of the layer in GIXRD, as show in Figure 8d, is also low of less than 0.8° . It is worth noting that the azimuthal mosaicity measured around the (202) reflection in standard configuration - probing the whole diamond crystal- is 0.9° (not shown here). This is consistent with an azimuthal mosaicity that decreases slowly during growth, as observed in [21].

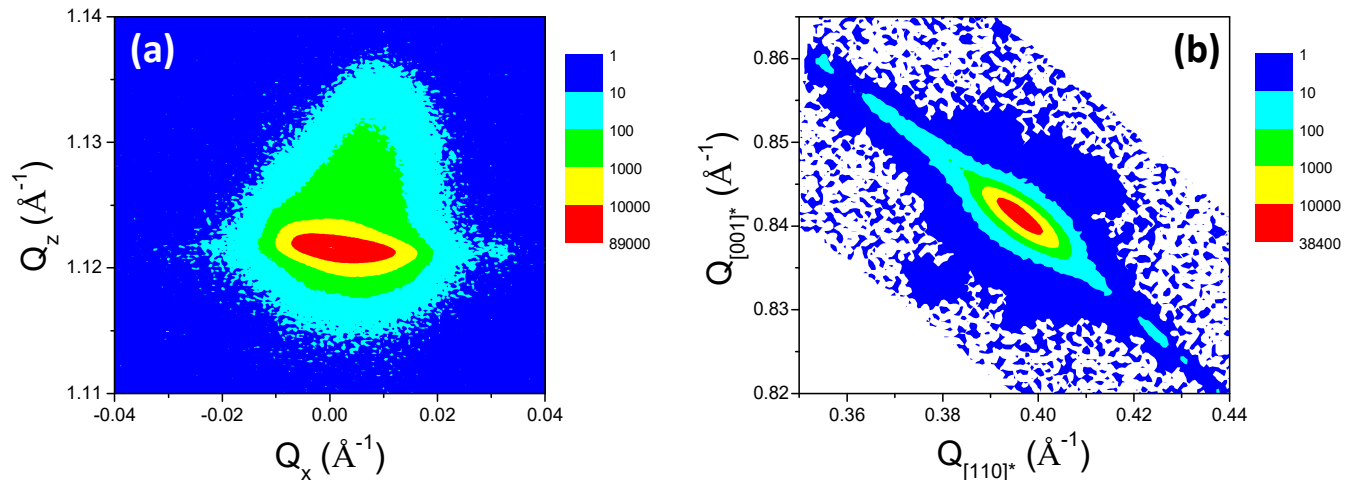


Figure 9 XRD reciprocal space maps from the epitaxial diamond layer on Ir/STO/Si(001) around (a) the (004) node, and (b) the (113) node.

Reciprocal Space Maps (RSMs) around the (004) and (113) nodes, shown on Figure 9, were recorded. Most of the diffracted intensity is located around the bulk Bragg positions, confirming that the diamond layer is mainly relaxed. In Figure 9a, the main intensity of the (004) node is located at $Q_z = 1.121 \text{ \AA}^{-1}$, corresponding to an out-of-plane cell parameter of $c = 3.568 \text{ \AA}$, equal to the bulk value within instrumental resolution. The elongated shape along Q_x of the main intensity of the (004) node is due to the 0.5° mosaicity, as observed above in Figure 8c. The residually strained diamond portion with lower cell parameters in the out-of-plane direction (centered at $c = 3.559 \text{ \AA}$) is visible in this map (tilted triangular shape above $Q_z = 1.121 \text{ \AA}^{-1}$). Q_x profiles done at different Q_z values (Fig. S3a) reveal a main tendency of the mosaicity with strain (Fig. S3b). The mosaicity tends to decrease with in-plane tensile strain (reduction of out-of-plane cell parameter), although minima are found for the relaxed diamond portion. Interestingly, a correlation is also shown between the strain and the tilt of the diamond crystals along the $<100>$ diamond direction with respect to the Si(001) planes (Fig. S3c). Roughly, negligible tilt ($<0.1^\circ$) is revealed around the relaxed diamond position whereas tilt tends to increase with strain (especially with in-plane tensile strain). Q_z profiles done at different Q_x values (Fig. S4a) confirm that the strained diamond portion is associated with a crystallographic tilt (Fig. S4b-c). In Figure 9b, the corresponding out-of-plane (c) and in-plane (a) lattice parameters measured from the main intensity of the asymmetrical RSM around the (113) node are $c = 3.567 \text{ \AA}$ and $a = 3.568 \text{ \AA}$, confirming that diamond layer is mainly relaxed along both the out-of-plane and in-plane directions.

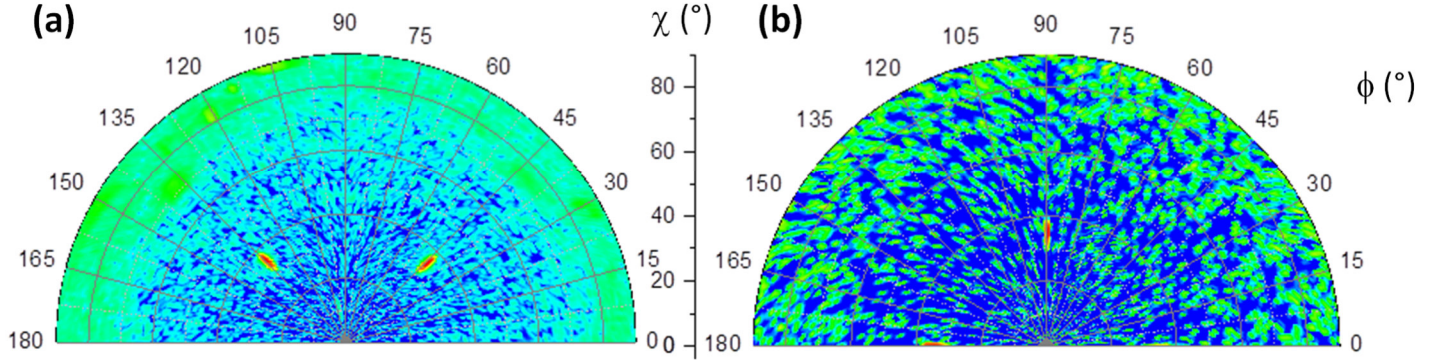


Figure 10 XRD half pole figures around (a) the (111) reflection of the diamond layer; (b) the (111) reflection of the silicon substrate.

Half pole figures ($0 \leq \phi \leq 180^{\circ}$) have been recorded to confirm the in-plane epitaxial relationship between the diamond layer and the Si substrate, and also to look at other possible diamond orientations, easily missed in a standard $\theta/2\theta$ scan. Figure 10a shows that the {111} reflections appear only two times at $\chi = 35.3^{\circ}$, spaced by 90° in ϕ (45° and 135°). These positions correspond to the (001)-oriented epitaxial diamond layer of four-fold in-plane symmetry. The fact that the {111} reflection does not appear at any other location indicates that diamond layer is fully epitaxial with (001) orientation, without crystal tilt and without crystal twinning. For comparison and to confirm the epitaxial relationship, Figure 10b shows the positions of the {111} reflections of the Si(001) substrate. The shift of 45° in ϕ (90° and 180°) with respect to the diamond layer confirms the epitaxial relationship in our heterostructure: $<100>$ diamond (001) // $<110>$ Si (001).

A look at CL emissions in the visible range provides a first overview of the defects present in the sample. CL and DiamondViewTM images of the sample are shown in Figs. 11b and 11c together with its optical view (Fig. 11a). A blue luminescence is observed, which is due to the A-band [22] as confirmed by the CL spectrum shown in Figure 11d.

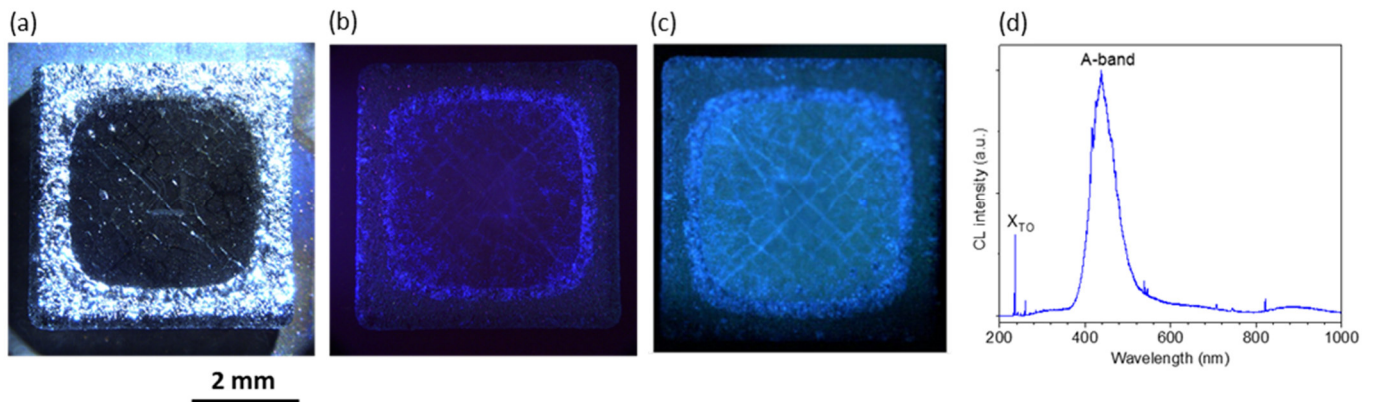


Figure 11 (a) Optical image of the thick diamond film grown on Ir/STO/Si (001) substrate. Besides are shown luminescence images in the visible range at 300K; (b) CL and (c) DiamondViewTM; (d) Typical CL spectrum taken at 10 K on the final growth surface in the 200-1000 nm range.

Deeper insights into the properties of the heteroepitaxial diamond have been achieved with a second level of analysis focused on the CL imaging of exciton recombinations at 235 nm. Such images can reveal single unitary dislocations in diamond as shown in [23]. More generally the dark points, lines or areas observed in the CL

images of the intrinsic recombinations reveal the presence of structural defects and their spatial organisation in semiconductor monocrystals. The experiments were performed here, either on the final surface or on the polished cross-section of the sample to better understand what holds on during the diamond growth process.

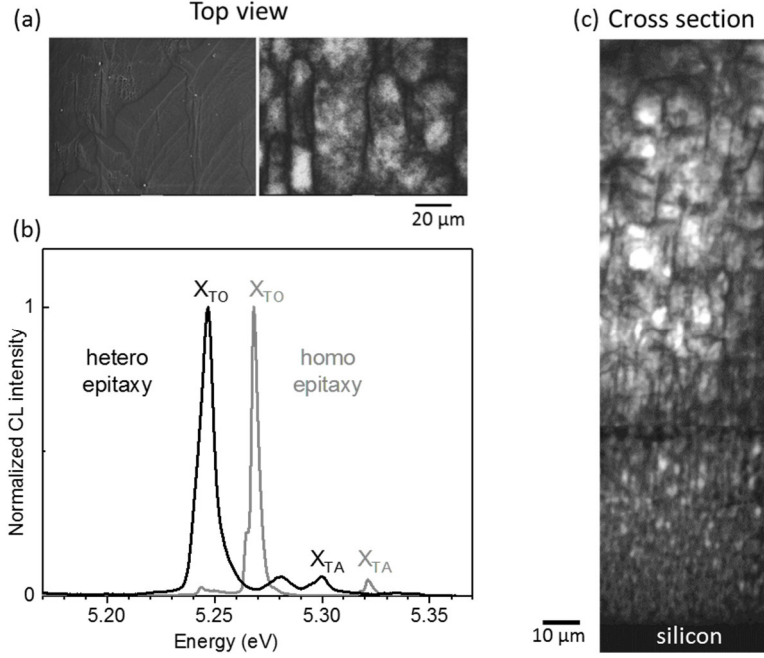


Figure 12 (a) SEM and CL images of free exciton recombination (X_{TO} filtered at 235 ± 3 nm) recorded from the surface; (b) Typical CL spectrum in the UV range observed at the surface, compared with a commercial homoepitaxial diamond layer (Element 6 electronic grade); (c) CL image of free exciton recombination (X_{TO} filtered at 235 ± 3 nm) of the cross-section of the heteroepitaxial layer.

The CL images taken from the final growth surface on Fig. 12a reveal that dislocations are organized in a network with variable cell sizes, as already evidenced in our previous work on heteroepitaxial diamond grown on bulk STO substrates [17].

A typical CL spectrum taken at the surface of the heteroepitaxial diamond is compared with a bulk crystal grown by CVD in homoepitaxy (Element 6 electronic grade) on the Fig. 12b. The dominant free exciton peak (X_{TO}) of the heteroepitaxial diamond appears shifted at low energy with respect to the reference single crystal, meaning the heteroepitaxial layer present residual strain at the surface. In some area at the diamond surface, the X_{TO} peak sometimes appears splitted, as observed in our previous work on bulk STO substrates [17]. This reveals a non-uniformity of the principal directions of residual stress at the crystal surface, which is probably related to the dislocation network. Such stress variations were also observed in micro Raman (c.f. Fig. S5).

Along the cross-section presented in Fig. 12c, we observe the propagation of dislocations during growth from the Ir/STO/Si (100) substrate to the diamond surface. Their propagation almost follows the [100] growth direction. Interestingly, the cell size clearly tends to increase during growth, with a dislocation density inside cells that decreases. Even if unitary dislocations are not resolved in Fig. 12c, the reduction of the dislocation density appears by the fact that the top cells are much brighter. This cross section analysis provides another illustration to the fact that the density of structural defects decreases during diamond growth, as observed by other groups [24].

3.4 Fabrication and characterization of lateral Schottky diodes on heteroepitaxial diamond

After polishing, the thickness of the heteroepitaxial diamond crystal grown on Ir/STO/Si (001) was reduced to 173 μm . It was used to grow a low boron doped epilayer, 1.6 μm thick, by CVD (details provided in the experimental section). After growth, the sample was cleaned by acid treatment to remove the graphitic layer that appeared on the backside. The morphology of the grown layer was characterized by optical profilometry (Fig S6), an average roughness of 30 nm was measured on a 1.17 mm^2 area and Pyramidal Hillocks (PH) were evidenced on the surface especially at the edges of the sample. These results are comparable to those currently obtained for this low doping level and thickness range on homoepitaxial substrates [25] meaning that the underneath epitaxial stacking does not significantly impact the growth of the boron doped layer, though its defect density is much higher.

Lateral Schottky diodes were defined on this boron doped layer avoiding the edges. In this architecture, both ohmic and Schottky contacts are located on the top layer, which is easier to realize. This constitutes a first way to evaluate the electronic performance of low-boron-doped epilayers grown on heteroepitaxial diamond. A lithography lift-off process was applied. Both ohmic and Schottky contacts were obtained by evaporation assisted by electron-beam. For the ohmic contact, titanium (30 nm), platinum (50 nm) and gold (40 nm) were deposited and for the Schottky contact, zirconium (20 nm), platinum (30 nm) and gold (10 nm). The design of these diodes is presented in Figure 13 with the final device picture. Cracks are visible on Fig. 13a, but according to optical profilometry, no cracks were present on the top surface (Fig. S6). This shows that these cracks are located underneath, probably near the diamond/Ir interface. The device design is composed of two identical areas, each containing a common ohmic contact with a 1.9 mm^2 surface area encircling Schottky contacts. The Schottky contacts are organized as an array of circular areas with different diameters: 200 μm (11 contacts), 100 μm (12 contacts), 40 μm (66 contacts) and 20 μm (66 contacts).

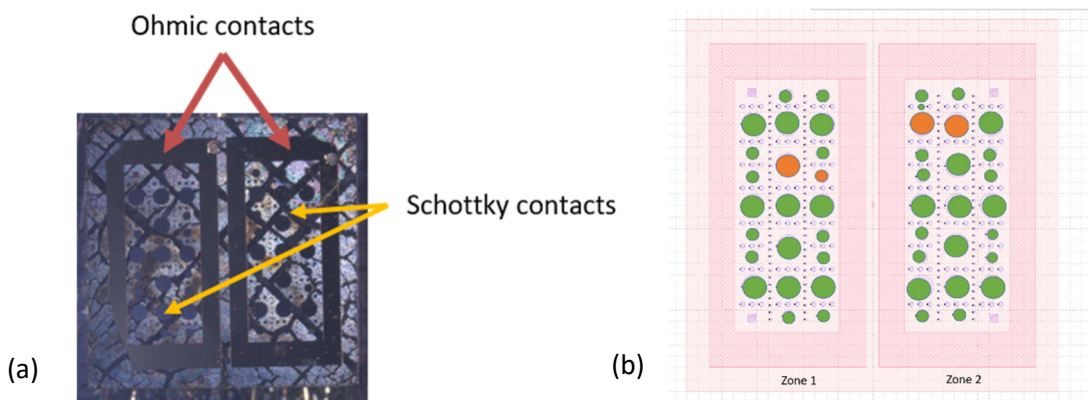


Figure 13 a) Optical image of the final device. Note that the cracks are located on the backside of the diamond crystal and seen by transparency (see details in the text); b) Mapping of the devices that present a diode behavior with rectification (in green) or (in orange) no rectification

I-V characteristics were measured when applying a bias ramp from -5 to 5 V to get the entire curve (both thermionic and ohmic parts). As the thermionic current was increased exponentially, a second measurement was done between 0 and 2 V to extract properly the effective barrier height (ϕ_b). The yield of the device fabrication process is defined as the number of working diodes (showing a rectification behavior) over the total number of devices. The yield on the heteroepitaxial diamond was up to 92 % as shown on Figure 13b, which is similar to

the yield generally obtained when the same devices are fabricated on homoepitaxial films on high quality HPHT diamond substrates (10^2 dislocations /cm²) [26]

The full I-V measurements recorded for 18 diodes are presented in Figure 14. It is already clear that the diode characteristics are highly uniform on the heteroepitaxial substrate.

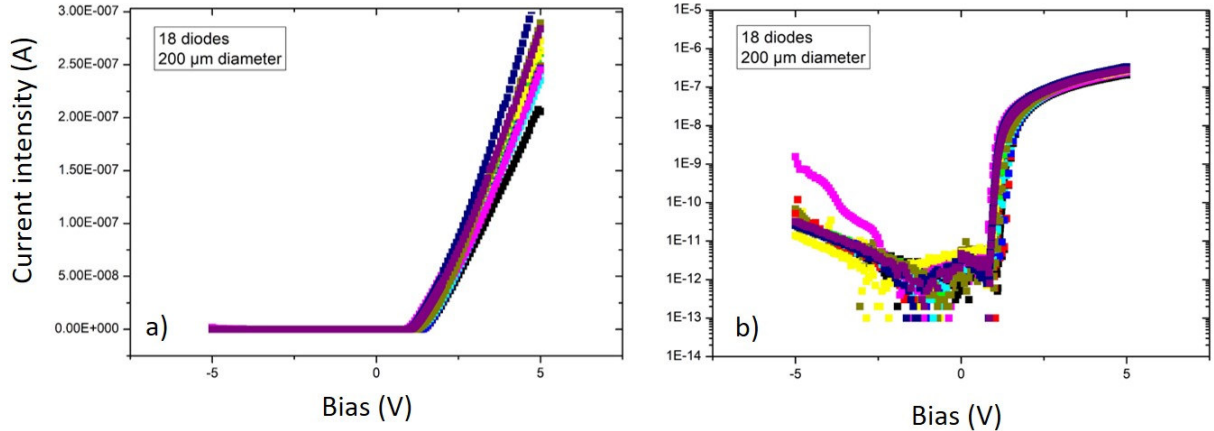


Figure 14: I-V characteristics of 18 diodes of 200 μm diameter at RT and under vacuum a) in linear scale; b) in logarithmic scale

The I-V analysis indeed shows that all Schottky diodes present the same effective barrier height and a serial resistance which varies only from 9.8 to 12.2 M Ω . The details of the analysis are given below.

First, a comment is deserved on the high value of the serial resistance, which is expected, given the low boron doping level of the active layer and the high contact resistance. The measurement between the two ohmic contacts indeed gives a 31120 Ω resistance.

For Schottky diodes, the forward current is analyzed with the following expression [27]:

$$I = I_s \exp\left(\frac{q(V-RI)}{nk_b T}\right) \left[1 - \exp\left(-\frac{q(V-RI)}{k_b T}\right)\right] \text{ with } I_s = A^* T^2 S \exp\left(\frac{-q\phi_b}{k_b T}\right)$$

With q the elementary charge, k_b the Boltzmann constant, T the temperature in Kelvin, V the applied bias, ϕ_b the Schottky barrier height, n the ideality factor, S the diode area, R the resistance and A* the effective Richardson constant equal to 90 A.cm⁻².K⁻².T [28].

Fitting the exponential part of the data led to determine the Schottky barrier height as well as the ideality factor. The extracted effective barrier height is $\phi_b = 1.45 \pm 0.05$ eV for all the diodes. The ideality factor n is close to 2 ($n = 1.85 \pm 0.2$) for each of them, meaning that the interface between diamond and the metallic contact may be improved.

Boron doping level homogeneity in-depth and laterally was also investigated via C-V measurements made randomly over the sample. The applied bias varied between -5 to 2 V with a frequency of 100 Hz. 1/C² vs. bias curves for seven diodes are presented on Figure 15. All curves showed the same slope demonstrating a good homogeneity of the sample. The linear behavior of the curve suggests a good doping uniformity of the grown epilayer in-depth. By fitting the linear part, the effective doping level of the boron doped layer could be extracted:

$$Na - Nd = \frac{-2}{q\epsilon_0\epsilon_s S^2 \frac{d(\frac{1}{C^2})}{dV}}$$

with ϵ_0 the vacuum permittivity, ϵ_s diamond permittivity 5.5, S the contact surface and $d(1/C^2)/dV$ extracted from the curve. An effective doping level of 1.3×10^{16} boron atoms.cm⁻³ was obtained which is expected for the used MPCVD conditions (see experimental part). Moreover, the Schottky diode built-in potential V_{bi} which is given when the linear fit is crossing the bias axe ($y = 0$) equal to 3.34 V. This is in good agreement with the targeted doping level for this grown layer.

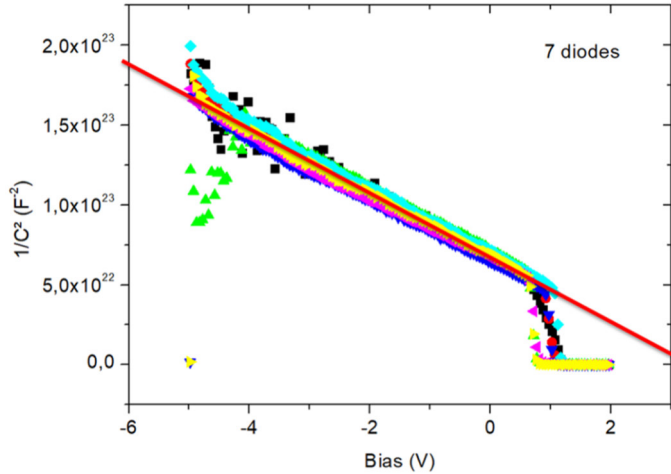


Figure 15: $1/C^2$ - V curves of 7 diodes from all over the sample and in red the linear fit

4. Discussion

4.1 HRTEM observations of diamond nanocrystals after BEN

During BEN, nucleation domains, i.e. areas containing diamond *nuclei*, are formed on iridium surfaces. Our HRTEM observations evidence the presence of nanocrystals in epitaxial relationship with iridium according to FFT analysis (Fig. 4a and 4b). STEM-EELS experiments performed on these nanocrystals revealed a clear diamond σ^* signature at the carbon K edge (Fig. 4c). From our knowledge, it is the first report of direct HRTEM observations of diamond nanocrystals after BEN on iridium surfaces. In previous investigations, such diamond nanocrystals were undetectable by HRTEM without applying a short CVD growth of 5 s [29]. Up to now, the diamond signature at this stage was detected either by X-ray Photoemission Diffraction (XPD) [30, 31] or by High Resolution EELS [32], in both cases without imaging evidence. This means that diamond nanocrystals with size up to 7 nm are stable under our BEN conditions, leading to epitaxial growth on Ir (001). This result supports our previous sequential FE-SEM study which identified the locations of diamond *nuclei* within domains [11]. This original finding compared to the literature could result from differences in nucleation mechanisms occurring during BEN, very dependent on the reactor geometry and the cathodic sheath generated under bias. During BEN, furrows are formed on iridium surfaces. Our previous observations with FE-SEM indicate that furrows are always coexisting with domains [11]. The diamond nanocrystal observed on the HRTEM picture depicted on Fig 4a is precisely located at a step edge present on the iridium surface, which might suggest such Ir step edge acts as a nucleation center for diamond. More statistics are obviously needed to conclude about this point on the role of furrows in the nucleation of diamond on iridium. According to lattice parameters measured from HRTEM, the diamond nanocrystal underwent an in-plane tensile strain of about +7% (Part 3.1). This value is much higher than

the experimental tensile strength for bulk diamond (lower than 1%). Such huge local tensile strain, up to 9%, was recently reported at nanoscale on single crystal diamond needles. For polycrystalline diamond needle, this local tensile strain is significantly lower, close to 3% [33].

4.2 Crystalline quality and strain for thin and thick heteroepitaxial films

Thin diamond film (310 nm)

The sensitivity of UV Raman to the first order Raman peak of diamond was already underlined for polycrystalline and monocrystalline films [34]. Indeed, the intensity ratio of diamond to non-diamond carbon is exalted using an UV excitation wavelength. In the present study, we applied UV Raman to characterize thin heteroepitaxial diamond films of 310 nm. The position of the first order diamond peak is detected at 1330 cm^{-1} down-shifted towards the relaxed reference (1332.5 cm^{-1}), corresponding to a mean strain in tension for the 310 nm heteroepitaxial film [20]. According to HRTEM, the diamond thin film appears to be completely relaxed. The down-shift of the Raman peak at 1330 cm^{-1} corresponds to a stress in the film of ca. 4 GPa. The Young modulus of diamond is 1000 GPa implying, in a purely elastic regime, a deformation of 0.4 % which means a variation of the unit cell parameter of 0.001 nm. This value is much smaller than the accuracy on the measurements of atomic distance from HRTEM imaging. Thus, even if the diamond thin film is strained, it is not possible to evidence it by electron microscopy. Moreover, the strain relaxation in thin films during samples preparation for electron microscopy is a well-known phenomenon [35] and can explain this apparent disagreement between the results obtained by Raman spectroscopy and TEM. Contrary to HRTEM which investigates local lattice deformations, the total thickness of the film contributes to the Raman signal.

The strain within the heteroepitaxial diamond film evolves during its growth. After BEN, isolated nanometric diamond crystals, formed at the interface, underwent a huge tensile strain (part 4.1). No plastic deformation can be detected on HRTEM images due to the uncertainty on interplanar spacings. During the coalescence of such nanocrystals, a higher strain is generated leading to the formation of dislocations to achieve a plastic relaxation. The presence of stacking faults inside the film (Fig. 7a and b) indicates this relaxation of the film. Moreover, the formation of cracks observed near the diamond/Ir interface (Fig. 13a) also support the strain relaxation.

240 μm thick diamond films

The crystalline quality of heteroepitaxial diamond on Ir/STO/Si (001) is similar to the one grown on Ir/STO (001). Ir/STO/Si (001) pseudo-substrates allow for up-scaling of heteroepitaxial diamond keeping similar crystalline quality and reducing in addition the thermal expansion mismatch between the diamond layer and the substrate. The thick epitaxial diamond layer is single crystalline and mainly relaxed, as observed by RSMs and pole-figures. Only a small part of the thick film (< 5%) is found to be slightly tensile-strained, (less than 0.2%), part which is most probably generated at the early stages of the growth, as suggested by CL results. The lattice of dislocations evolves during growth of a thicker heteroepitaxial diamond film, it arranges into cells observed in CL close to the surface (Figure 12c), resulting from dislocations aggregation in larger columns. Strain and deformations observed locally at the surface result from the presence of this lattice of dislocations.

4.3 Transport properties of lateral Schottky diodes grown onto heteroepitaxial substrate

Those measurements are promising, with a good fabrication yield, equal to 92% and showing a good reproducibility of device fabrication all over the substrate surface. The Schottky barrier height extracted from this diode is in good agreement with that obtained for the same process on homoepitaxial films [26]. Unfortunately, the ideality factor close to 2 means that the interface between diamond and the metallic contact is not as good as expected. As shown by Muret et al [36], interface state at the junction between zirconium and diamond can induce an increase of the ideality factor. Nevertheless, dislocations coming vertically from the

grown layer do not affect the good diode characteristic due to the lateral architecture chosen for this device. The drawback of this geometry is the long distance between Schottky and ohmic contacts inducing a high resistance and limiting the forward current and likely the breakdown voltage even if is not measured on this sample. C-V measurements confirm the successful boron incorporation to a similar level as expected in a homoepitaxial film. All these remarks lead us to believe that the influence of dislocations is very anisotropic on the electrical characteristics of diodes. In the volume, the absence of a short circuit between the two contacts shows that the current lines are mainly perpendicular to the dislocations and that they do not affect the resistance of the diode that much. Unfortunately, dislocations keep a major influence on the interface with Schottky metal with a strong barrier inhomogeneity. Thus, the use of heteroepitaxial layers to produce electronic components is demonstrated, it will be necessary to develop new geometries to overcome the influence of defects still inherent in this material. Further work to reduce the presence of defects through optimization of the different growth steps will also need to be carried out.

5. Conclusion

Structural and chemical investigations were performed after each step of the heteroepitaxy process applied to Ir/STO/Si(001) substrates. HRTEM and STEM-EELS observations revealed that nanometric diamond epitaxial crystals are stable under our BEN conditions. No comparable observation has been reported before. After the growth of a thin film (310 nm), a direct epitaxy of diamond on iridium was observed without an intermediate layer. A compressive strain was localized at the interface with iridium and released at 100 nm from the interface. After the strain became compressive. This is in line with the observed shift on the UV Raman spectra. The thick diamond film grown under CVD conditions used for homoepitaxy is mainly relaxed (less than 5 % of the diamond layer has a residual strain of around 0.2 %). CL investigations revealed a network of dislocations cells which propagated along [100] growth direction, the cell size increased with the film thickness.

Lateral Schottky diodes were fabricated on a polished 173 μm -thick heteroepitaxial film with a thin boron-doped epilayer. I-V characteristics evidenced a yield of working diodes equal to 92%, close to that obtained for diodes on homoepitaxial films. Despite a higher expected defect density, when heteroepitaxial diamond is used as a substrate, the active layer doping and the device characteristics (serial resistance, Schottky barrier and ideality) appear highly uniform. The lateral device tested might be a favorable architecture with respect to threading dislocations, but the results obtained here and in the literature [37, 38] support the use of heteroepitaxial diamond for large area electronic devices. The investigation of power devices based on this material is thus desired in the future. Growth strategies promoting ELO are currently under investigations to further improve the crystalline structure of heteroepitaxial diamond films grown on Ir/STO/Si(001) substrates.

Acknowledgments

Authors thank the French ANR agency and DGA for funding through the DIAMWAFEL project (ANR-15-CE08-0034).

References

- [1] K. Ichikawa, K. Kurone, H. Kodama, K. Suzuki, A. Sawabe, High crystalline quality heteroepitaxial diamond using grid patterned nucleation and growth on Ir, *Diam. Relat. Mater.* 94 (2019) 92.
- [2] M. Schreck, S. Gsell, R. Brescia, M. Fischer, Ion bombardment induced buried lateral growth: the key mechanism for the synthesis of single crystal diamond wafers, *Scientific Reports* (2017) 7:44462.
- [3] K. H. Lee, S. Saada, J. C. Arnault, R. Moalla, G. Saint-Girons, R. Bachelet, H. Bensalah, I. Stenger, J. Barjon, A. Tallaire, J. Achard, Epitaxy of iridium on SrTiO₃/Si (001): A promising scalable substrate for diamond heteroepitaxy, *Diam. Rel. Mater.* 66 (2016) 67.
- [4] S. W. Kaun, M. H. Wong, U. K Mishra, J. S. Speck, Molecular beam epitaxy for high-performance Ga face GaN electron devices, *Semicond. Sci. Technol.* 28 (2013) 074001.
- [5] S. J. Pearson, F. Ren, E. Patrick, M. E. Law, A. Y. Polyakov, Review—Ionizing Radiation Damage Effects on GaN Devices, *ECS Journal of Solid State Science and Technology*, 5 (2016) Q35-Q60.
- [6] Y. Wei, X. Hu, Y. Liang, D. C. Jordan, B. Craig, R. Droopad, Z. Yu, A. Demkov, J. L. Edwards Jr, W. J. Ooms, Mechanism of cleaning Si(100) surface using Sr or SrO for the growth of crystalline SrTiO₃ films, *J. Vac. Sci. Technol. B* 20 (2002) 1402.
- [7] G. Saint Girons, R. Bachelet, R. Moalla, B. Meunier, L. Louahadj, B. Canu, A. Carretero-Genevrier, J. Gazquez, P. Regreny, C. Botella, J. Penuelas, M. G. Silly, F. Sirotti, G. Grenet, Epitaxy of SrTiO₃ on Silicon: The Knitting Machine Strategy, *Chem. Mater.* 28 (2016) 5347.
- [8] G. Niu, B. Vilquin, J. Penuelas, C. Botella, G. Hollinger, G. Saint-Girons, Heteroepitaxy of SrTiO₃ thin films on Si (001) using different growth strategies: Toward substrate like quality, *J. Vac. Sci. Technol. B* 29 (2011) 041207.
- [9] C. Baeumer, C. Xu, F. Gunkel, N. Raab, R. A. Heinen, A. Koehl, R. Dittmann, Surface Termination Conversion during SrTiO₃ Thin Film Growth Revealed by X-ray Photoelectron Spectroscopy, *Sci. Rep.* 5 (2015) 11829.
- [10] R. Bachelet, F. Sanchez, F. J. Palomares, C. Ocal, J. Fontcuberta, Atomically flat SrO-terminated SrTiO₃(001) substrate, *APL* 95 (2009) 141915.
- [11] N. Vaissiere, S. Saada, M. Bouttemy, A. Etcheberry, P. Bergonzo, J.C. Arnault, Heteroepitaxial diamond on iridium: new insights on domain formation, *Diam. Relat. Mater.* 36 (2013) 16.
- [12] R. Moalla, B. Vilquin, G. Saint-Girons, G. Sebald, N. Baboux, R. Bachelet, Dramatic effect of thermal expansion mismatch on the structural, dielectric, ferroelectric and pyroelectric properties of low-cost epitaxial PZT films on SrTiO₃ and Si, *Cryst. Eng. Comm.* 18 (2016) 1887.
- [13] D. Han, M. Bouras, C. Botella, A. Benamrouche, B. Canut, G. Grenet, G. Saint-Girons, R. Bachelet, Poisson ratio and bulk lattice constant of (Sr_{0.25}La_{0.75})CrO₃ from strained epitaxial thin films, *J. Appl. Phys.* 126 (2019) 085304.
- [14] M. Schreck and J. C. Arnault, Heteroepitaxy of diamond on Ir/metal-oxide/ Si substrates in Power Electronics Device Applications of Diamond Semiconductors, S. Koizumi, H. Umezawa, J. Pernot and M. Suzuki Eds, Elsevier (2019) ISBN: 9780081021835
- [15] A. Chavanne, J. Barjon, B. Vilquin, J. Arabski, J.C. Arnault, Surface investigations on different nucleation pathways for diamond heteroepitaxial growth on iridium, *Diam. Relat. Mater.* 22 (2012) 52.

- [16] J. Achard, F. Silva, A. Tallaire, X. Bonnin, G. Lombardi, K. Hassouni, A. Gicquel, High quality MPACVD diamond single crystal growth: High microwave power density regime, *J. Phys. D* 40 (2007) 6175.
- [17] H. Bensalah, I. Stenger, G. Sakr, J. Barjon, R. Bachelet, A. Tallaire, J. Achard, N. Vaissière, K. H. Lee, S. Saada, J. C. Arnault, Mosaicity, dislocations and strain in heteroepitaxial diamond grown on iridium, *Diam. Rel. Mater.* 66 (2016) 188.
- [18] J. Barjon and K. Haenen Optical spectroscopy for doped diamond Layers in Power Electronics Device Applications of Diamond Semiconductors, S. Koizumi, H. Umezawa, J. Pernot and M. Suzuki Eds, Elsevier (2019) ISBN: 9780081021835
- [19] S. Turner, Structure, shape, defects and impurities in nanodiamonds investigated by HRTEM and STEM-EELS in Nanodiamonds, J.C. Arnault Ed, Elsevier (2017) ISBN 978-0-323-43029-6.
- [20] Y. von Kaenel, J. Stiegler, J. Michler, E. Blank, Stress distribution in heteroepitaxial chemical vapor deposited diamond films, *J. Appl. Phys.* 81 (1997) 1726.
- [21] M. Schreck, F. Hörmann, H. Roll, J.K.N. Lindner, B. Stritzker, Diamond nucleation on iridium buffer layers and subsequent textured growth: A route for the realization of single-crystal diamond films, *Appl. Phys. Lett.*, 78 (2001) 192.
- [22] A. M. Zaitev, Optical Properties of Diamond, Springer, 2001. ISBN: 978-3-540-66582-3
- [23] A. Tallaire, T. Ouisse, A. Lantreibecq, R. Cours, M. Legros, H. Bensalah, J. Barjon, V. Mille, O. Brinza, J. Achard, Identification of dislocations in synthetic chemically vapor deposited diamond single crystals, *Crystal Growth and Design*, 16 (2016) 2741.
- [24] M. Schreck, M. Mayr, O. Klein, M. Fischer, S. Gsell, A. Frota Sartori, B. C. Gallheber, Multiple role of dislocations in the heteroepitaxial growth of diamond: A brief review, *Phys. Status Solidi A* 213 (2016) 2028.
- [25] A. Tallaire, M. Kasu, K. Ueda, T. Makimoto, Origin of growth defects in CVD diamond epitaxial films, *Diam. Relat. Mater.* 17 (2008) 60–65.
- [26] A. Traoré, P. Muret, A. Fiori, D. Eon, E. Gheeraert, J. Pernot, Zr/oxidized diamond interface for high power Schottky diodes, *Appl. Phys. Lett.* 104 (2014) 052105.
- [27] S.M. Sze, K.K. Ng, J.-P. Colinge, C.A. Colinge, Physics of Semiconductor Devices, J. Willey and Sons, 2006.
- [28] H. Umezawa, T. Saito, N. Tokuda, M. Ogura, S.G. Ri, H. Yoshikawa, S.I. Shikata, Leakage current analysis of diamond Schottky barrier diode, *Appl. Phys. Lett.* 90 (2007) 073506.
- [29] R. Brescia, M. Schreck, S. Gsell, M. Fischer, B. Stritzker, Transmission electron microscopy study of the very early stages of diamond growth on iridium, *Diam. Relat. Mater.* 17 (2008) 1045.
- [30] S. Kono, T. Takano, T. Goto, Y. Ikejima, M. Shiraishi, T. Abukawa, T. Yamada, A. Sawabe, Effect of bias treatment in the CVD diamond growth on Ir(001), *Diam. Relat. Mater.* 13 (2004) 2081.
- [31] S. Gsell, S. Berner, T. Brugger, M. Schreck, R. Brescia, M. Fischer, et al., Comparative electron diffraction study of the diamond nucleation layer on Ir(001), *Diam. Relat. Mater.* 17 (2008) 1029.
- [32] A. Hoffman, S. Michaelson, R. Akhvlediani, N.K. Hangaly, S. Gsell, R. Brescia, M. Schreck, B. Stritzer, J. C. Arnault, S. Saada, Comparison of diamond bias enhanced nucleation on Ir and 3C-SiC: A high resolution electron energy loss spectroscopy study, *Phys. Status Solidi A* 206 (2009) 1972.

- [33] A. Banerjee, D. Bernoulli, H. Zhang, M. F. Yuen, J. Liu, J. Dong, F. Ding, J. Lu, M. Dao, W. Zhang, Y. Lu, S. Suresh, Ultralarge elastic deformation of nanoscale diamond, *Science* 360 (2018) 300.
- [34] S. Prawer and R. J. Nemanich, Raman spectroscopy of diamond, *Phil. Trans. R. Soc. Lond. A* 362 (2004) 2537.
- [35] F. Ahmed, M. Krottenthaler, C. Schmid, K. Durst, Assessment of stress relaxation experiments on diamond coatings analyzed by digital image correlation and micro-Raman spectroscopy, *Surf. Coat. Technol.* 237 (2013) 255.
- [36] P. Muret, A. Traore, A. Maréchal, D. Eon, J. Pernot, J. C. Pinero, M. P. Villar, D. Araujo, Potential barrier heights at metal on oxygen-terminated diamond interfaces, *J. Appl. Phys.* 118, (2015) 204505.
- [37] D. Takeuchi, T. Makino, H. Kato, M. Ogura, N. Tokuda, T. Matsumoto, D. Kuwabara, H. Okushi, S. Yamasaki, Free exciton luminescence from a diamond p–i–n diode grown on a substrate produced by heteroepitaxy, *Phys. Status Solidi A* 211 (2014) 2251.
- [38] H. Kawashima, H. Noguchi T. Matsumoto, H. Kato, M. Ogura, T. Makino, S. Shirai, D. Takeuchi, S. Yamasaki, Electronic properties of diamond Schottky barrier diodes fabricated on silicon-based heteroepitaxially grown diamond substrates, *Applied Physics Express* 8 (2015) 104103.